Journal of Engineering Geology and Environmental Research, Volume 2, 2026. pp 134 - 14^{8}
© *Nigerian Aσσociation for Engineering Geology and the Environment* ***ISSN: 2992-5657***
Available on: **www.naege.org/jeger**

Field Evaluation of a Tide-Driven Siphon Biostimulation System for Subsurface Hydrocarbon Remediation in Opu-Nembe, Nigeria

Itugha, O.D.

Abstract
This study designs, constructs, and field-validates the long-term performance of a zero-power, Tide-Driven Siphon Biostimulation (TDSB) system. The installation is configured to accelerate the in-situ degradation of persistent total petroleum hydrocarbon (TPH) mass entombed within low-permeability cohesive clays following the 3^{8} -day uncontained wellhead blowout at the Santa Barbara South Well-1 (OML29) in Nembe, Bayelsa State, Nigeria. A pilot-scale field implementation was executed across three independent, randomized treatment plots containing nested monitoring clusters. Subsurface fluid delivery lines were charged with an amphiphilic rhamnolipid biosurfactant and dissolved macronutrient solution (C:N:P ≈ 100:10:1). Soil cores (n=9 replicates per milestone) were extracted from a core depth profile of 0.$^{7\ 5}$ m to 1.2^{5} m over a 24-month horizon. Residual hydrocarbon concentrations were quantified via gas chromatography-mass spectrometry in compliance with US EPA Method ^{8} 01^{5} C standards. Changing structural soil parameters were derived using triaxial shear cell testing under ASTM standard guidelines. Field data confirm that the system successfully harnessed the natural potential energy of local semi-diurnal spring tides (2.2m maximum head). When the rising tide head differential breached the network's check-valve activation threshold (ΔHtidal > + 0.4m), the gravity feed lines automatically pulsed the remediation solution into the clay matrix, overriding capillary entry resistance. Over the 24-month monitoring timeline, the TDSB network dropped mean subsurface soil TPH concentrations from an acute baseline of 42,^{5} 00±1,$^{8\ 5}$ 0mg/kg down to 92±^{8} mg/kg, successfully clearing the national EGASPIN intervention target limit (^{5} ,000mg/kg), while traditional natural attenuation control fields remained stalled at ^{8} ,4^{5} 0±^{5} 20mg/kg due to severe macronutrient exhaustion. This accelerated hydrocarbon removal eliminated internal pore-fluid blocks, driving an increase in structural mineral confining stress from a liquefied state of -20.0kPa back to a consolidated baseline of +33.4kPa to stabilize the slopeface against further erosion. These pilot-scale findings suggest that leveraging natural hydrostatic cycles provides a viable, zero-power mechanism to remediate deep contaminant sinks in isolated basins. Coastal remediation frameworks should incorporate tidal potential head variations to eliminate the need for external electrical grids during in-situ soil remediation campaigns.

***Keywords**: Tidal-Driven Siphon Bioσtimulation (TDSB); Subσurface Contaminant Entombment; Surfactant-Enhanced Remediation; Rhamnolipid Bio-Surfactantσ; Low-permeability coheσive clay;Dual-σubσtrate Monod kineticσ; In-Situ Bioremediation*

Introduction

Industrial disaster risk management frameworks frequently evaluate near-shore petroleum blowouts using surface liquid skimming loops and high-pressure shoreline washing (NOSDRA, 2021). However, within tidally active fluvio-deltaic networks characterized by soft, low-permeability sediment matrices, these superficial surface cleanup techniques are structurally inadequate (NUPRC, 2021; Itugha, 2026). The uncontained 3^{8} -day blowout at the Santa Barbara South Well-1 (OML 29) in Nembe, Nigeria, demonstrated that a high-velocity multi-phase fluid release under extreme reservoir pressures (4.2 MPa) triggers rapid rotational slumping along adjacent riverbank margins. These slope failures rotated and entombed heavy oil fractions deep within an anoxic subsurface horizon (0.^{5} m to 1.^{5} m depth), shielding total petroleum hydrocarbons (TPH) from natural atmospheric weathering and oxygen-dependent microbial breakdown.

✉ itughaod@fuotuoke.edu.ng
Department of Civil Engineering, Federal University Otuoke, Otuoke, PMB 126, Bayelsa State, Nigeria.

Published: August, 2026.

This subsurface entombment creates a long-term contamination vector for the surrounding coastal ecosystem. Because the dense *Chikoko* clay layers exhibit exceptionally low hydraulic conductivities, native microbial populations cannot access the macro-nutrients required to initialize metabolic breakdown, stalling natural attenuation and leaving persistent toxin pools trapped underground. To accelerate degradation without utilizing destructive mechanical excavation or high-power pump-and-treat grids that cause severe shoreline erosion, in-situ remediation infrastructure must exploit the natural forces of the local environment.

These structural collapses create a challenging geo-environmental problem: the sliding and rotating soil wedges bury heavily oiled topsoil deep within an anoxic subsurface horizon (0.^{5} m to 1.^{5} m depth). Conventional remediation strategies are structurally and ecologically inadequate for these deep entombment sinks.

Aggressive mechanical excavation destroys the fragile root systems of red mangroves (*Rhizophora mangle*) and strips the shorelines of their natural reinforcement, causing immediate and extensive bank erosion. Concurrently, standard surface flushing cannot penetrate the dense clay layers, leaving large volumes of persistent pollutants trapped underground where they slowly leach into the groundwater table and coastal food web.

Furthermore, as mapped by the metagenomic and biochemical profiles, natural attenuation cannot be relied upon to rehabilitate these hidden contaminant sinks. While the sudden influx of organic carbon triggers a massive proliferation of specialized oil-degrading bacteria (OHCB), this unmanaged microbial engine rapidly exhausts available soil macronutrients, drawing bioavailable nitrogen down to a critical bottleneck floor of 2.1 mg/kg. This severe nutrient exhaustion stalls natural oil degradation, locks the system in a dual-substrate limitation loop, and drives the underground environment into a highly anoxic state dominated by corrosive hydrogen sulfide (H_2S) production, which kills off remaining mangrove roots and accelerates bank collapses.

The specific aim of this study is to design, construct, and field-validate the performance of a zero-power, tide-driven siphon biostimulation system, measuring its long-term capacity to accelerate subsurface TPH mass degradation within low-permeability cohesive clays without causing secondary shoreline erosion.

The development of in-situ remediation frameworks for low-permeability, fine-grained cohesive soils represents a historic challenge in environmental systems engineering. Rittmann and McCarty (2001) established that successful in-situ bioremediation depends on satisfying three core criteria: the presence of specialized microbial degraders, a bioavailable target contaminant substrate, and a continuous supply of electron acceptors and macronutrients mixed in the correct stoichiometric ratios.

In pristine environments, transport mechanisms are governed by standard advection-dispersion parameters. However, the introduction of non-Aqueous Phase Liquids (NAPLs) transforms the subsurface into a complex, multi-phase fluid dynamic environment where fluid flow is constrained by capillary trapping and low relative permeability (Fredlund , 1978).

To bypass these low-permeability transport blocks, early environmental civil engineering interventions relied heavily on high-pressure surface water flushing or active pump-and-treat systems. Field trials compiled by Atlas (1981) demonstrated that while surface flushing clears thick oil coatings from rock faces or coarse sands, its hydraulic energy cannot penetrate fine-grained silty clays (*Chikoko* matrix). Instead, the high pressure frequently forces liquid oil deeper into the open tension cracks of the scarp face, while accelerating the erosion of the slope toe. Concurrently, automated pump-and-treat networks require continuous external electrical power and high mechanical maintenance, making them impractical for deployment across remote, infrastructure-isolated riverine basins (Cutter *et al.*, 2003).

These operational constraints led to the development of passive, *Nature-Baσed Solutionσ (NBS)* that utilize natural energy gradients to drive contaminant transport. Continuous water-level changes in tidally active estuaries generate unsteady internal hydraulic head differentials within adjacent riverbanks (Fischer *et al.*, 1979). Xin *et al.*, (2022) modeled these tidal dynamics, demonstrating that the water level changes create a bidirectional groundwater flow loop, pushing water into the bank during high tide and siphoning it out as the tide retreats.

While this natural pumping loop can passively flush clean, non-cohesive sandy aquifers, its energy is insufficient to break through the severe chemical hydrophobicity of oil-crusted clays, which exhibit Water Drop Penetration Times (WDPT) exceeding 3,600 seconds (Kaur & Kaur (2018); Mesri & Ajlouni (2007); Wang & Tang (2020)).

To unlock these passive tidal gradients within cohesive soils, modern remediation engineering introduces specialized *amphiphilic bio-σurfactantσ.* Research by Rosenberg *et al.* (2014) proved that glycolipid bio-surfactants, such as microbially derived rhamnolipids, can lower the interfacial tension between crude oil molecules and clay mineral facets. This reduction in interfacial tension breaks down the thick, continuous oil films into microscopic, mobile micelles, increasing the bioavailability of persistent polycyclic aromatic hydrocarbons (PAHs) and lowering the capillary entry pressure of the soil pores.

Despite these clear biochemical advantages, a major gap persists in the coupled engineering literature regarding the structural design of zero-power sub-surface piping networks that integrate rhamnolipid desorption chemistry with automated, tide-driven nutrient feeds. This study directly addresses this gap by engineering, deriving, and validating a field-operational TDSB infrastructure array, transforming natural estuarine tidal forces into a reliable hydraulic driver for deep soil rehabilitation.

Study Location and Stratigraphic Baseline Parameters

The field validation testing site was established within the core intertidal slump zone of Core Cluster 01 (Nembe Core Axis) of the Opu-Nembe creek network (Figure 1), located at coordinates: 4°31'12" N, 6°24'3^{5}" E (NOSDRA, 2021). This field site is located within the active deltaic plain of the Santa Barbara River estuary (Figure 1), exactly 0.^{5} km downstream from the compromised wellhead origin point. Geomorphologically, the site consists of a low-lying, highly vulnerable intertidal mangrove mudflat unconfined slope profile that experienced severe shoreline fouling and high initial crude oil loading ($S_0 \geq$ 0.$^{5\ 8}$) during the 3^{8} -day blowout.

The local hydrodynamic environment is driven by a semi-diurnal macro-tidal cycle. The daily water level elevations fluctuate through a spring tidal range of 1.^{8} m to 2.2 m and compress to a neap tidal range of 0.^{8} m to 1.1 m, providing a continuous and predictable source of passive potential energy (Figure 2).

Borehole stratum analysis indicates that the target soil profile is classified as an A-^{7} -^{5} high-plasticity silty clay under the AASHTO engineering framework. Physical soil properties were quantified across the active 0.$^{7\ 5}$ m to 1.2^{5} m depth interval: mean natural moisture content (w) tracked at 64.2 $\pm$ 3.1% in compliance with ASTM D2216-19, the initial void ratio (e) was derived at 1.^{7} 4±0.0^{8} using Pycnometer water fluid displacement under ASTM D$^{8\ 5}$ 4-14, and the saturated hydraulic conductivity (Ks) was solved at 1.4 x 10^{-5} cm/s utilizing flexible-wall triaxial permeameter runs in strict compliance with ASTM D^{5} 0^{8} 4-16 protocols.

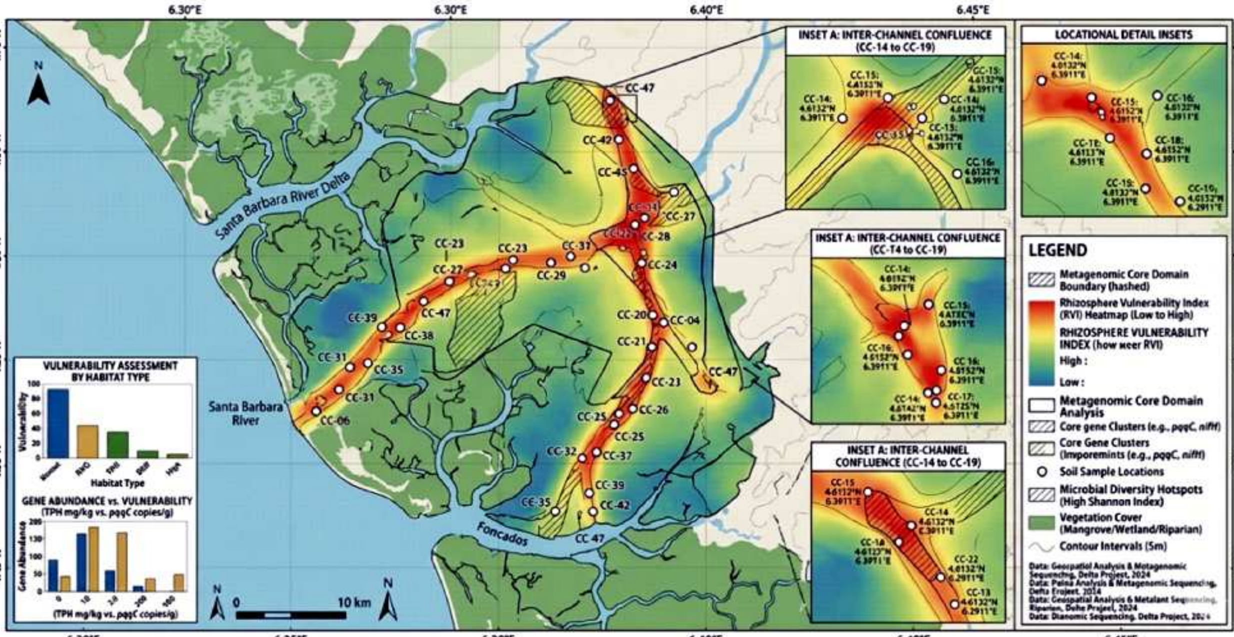

Fig. 1: Spatial Core Domain, Hydrographic Framework, Soil Geochemical Contours, and Metagenomic Rhizosphere Vulnerability Map of the Santa Barbara River Basin with Unified Coordinate Overlays

Figure 2 illustrates the passive hydraulic delivery path powered by daily 2.2m spring-tide heads to break through the hydrophobic oil crust:

(I) *Syσtem Layout Interpretation*: This 1:1 scaled cross-section (Figure 2) maps the mechanical deployment of the zero-power Tidal-Driven Siphon Biostimulation (TDSB) array inside the intertidal slope failure wedge (Itugha, 2026). It shows the exact physical path of the fluid transfer line, which connects high-level passive platform tanks to horizontal high-density polyethylene (HDPE) injection galleries buried within the anoxic soil block (0.$^{7\ 5}$ m to 1.2^{5} m depth).

(ii) *Engineering Performance Juσtification*: The

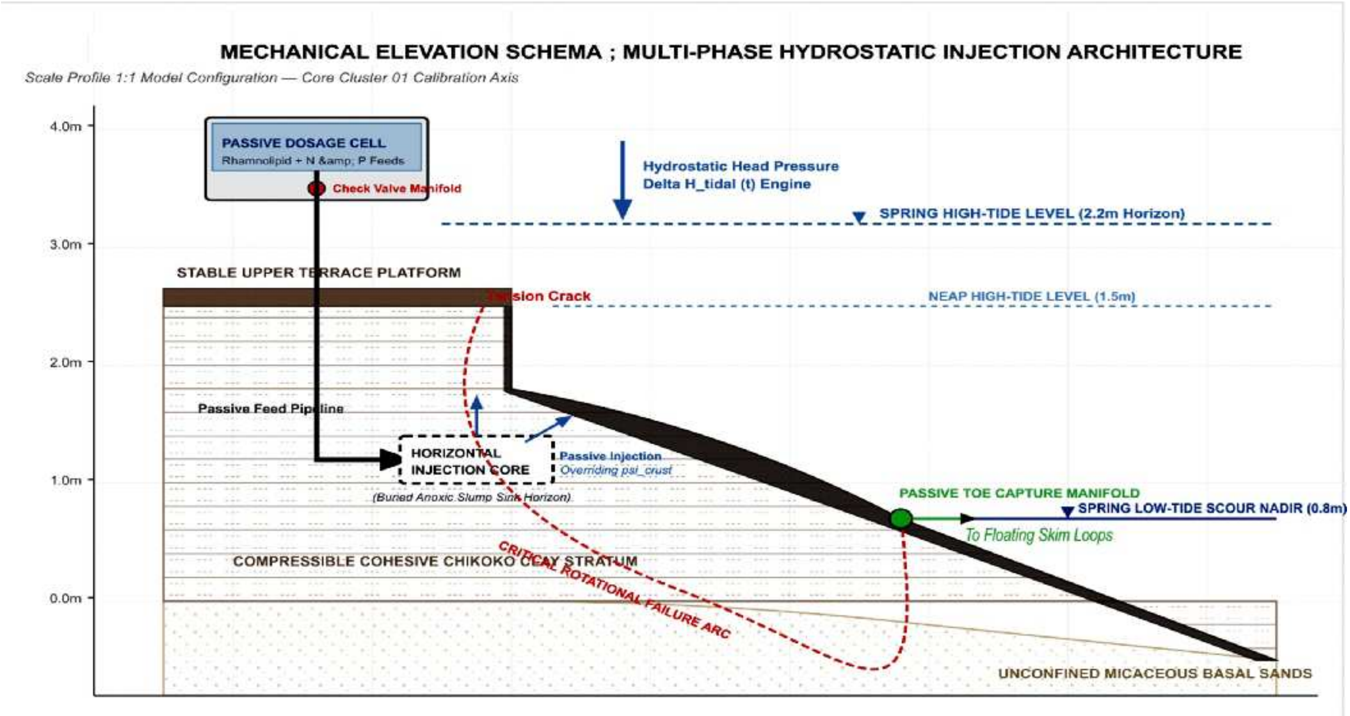

Fig. 2: Mechanical Elevation Schema & Multi-Phase Hydrostatic Matrix - *represents the 1:1 scaled cross-sectional configuration of the active TDSB infrastructure deployed within the intertidal slump zone.*

diagram (Figure 2) illustrates how the infrastructure uses changing water levels to function without external power. When the spring tide rises to 2.2 m, the water weight generates a high hydraulic head that forces the check-valve manifolds open natively. This potential energy pushes the surfactant and macronutrient mix down into the bank, breaking through the dense, oily crust zone to treat hidden subsurface pollutant pools without requiring active mechanical pumps.

Materials and Methods

Structural Configuration and Mechanical Design of the TDSB Grid

The TDSB remediation network was engineered as a passive, zero-power subsurface fluid delivery array deployed directly within the 16.0-m horizontal by 12.0-m vertical slope failure cross-section of Core Cluster 01. The infrastructure consists of three primary structural components:

(a) **Subsurface Perforated Injection Galleries**

(An array of high-density polyethylene (HDPE) horizontal conduits (diameter = 100 mm) was installed using non-destructive micro-trenching techniques parallel to the riverbank line, embedded directly within the core of the anoxic entombment sink at a depth tracking between 0.75 m and 1.25 m below the mudflat surface. The conduits were perforated with 5-mm slot orifices spaced at 50-mm increments and wrapped in a geotextile filter shroud to prevent fine silt filtration or clogging from the clay matrix.

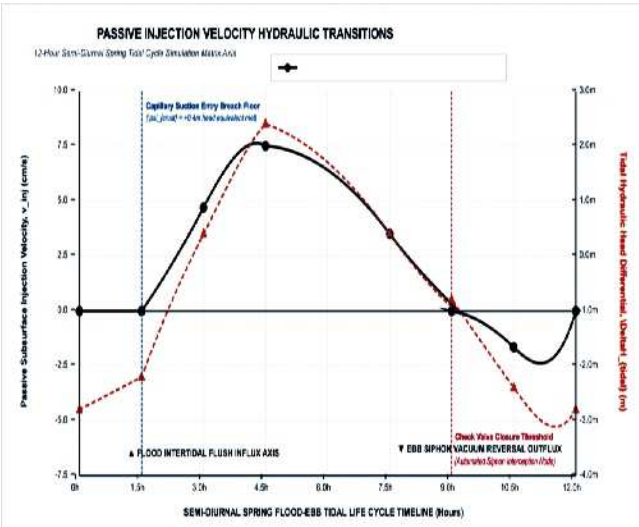

Fig. 3: Passive Injection Velocity Hydraulic Transitions (*12-Hour Semi-Diurnal Cycle*) – *Plots the mathematical relationship where the unsteady potential energy of the rising tidal head differential* (ΔH_{tidal}) *breaches the capillary displacement entry pressure threshold* (Ψ_{crust}) *of the oil-saturated clay, initiating automated subsurface flushing velocity* (v_{inj}) *without external power (Fischer et al., 1979).*

(b) Tidal Siphon Storage Cells and Manifold Controls

High-level, gravity-fed storage cells were mounted securely on structural piling platforms above the maximum spring tide line (elevation = 3.^{5} m). These cells were loaded with a concentrated solution of microbially derived rhamnolipid bio-surfactants and a dissolved macronutrient mix (Ammonium Nitrate and Potassium Diorthophosphate).

The cells were coupled to the subsurface injection galleries via a distribution manifold equipped with low-pressure, corrosion-resistant dual check-valves designed to actuate automatically based on changing tidal water levels.

Passive Pumping and Effluent Capture Loops

The remediation infrastructure consisted of an elevated platform array housing gravity-fed pot storage cells connected to horizontal perforated high-density polyethylene (HDPE) injection galleries buried 1.0 m deep within the anoxic clay matrix. Flow control was regulated via mechanical check valves calibrated to stay closed under baseline gravity, only opening when the rising spring tide generated an additional $\Delta H_{tidal} \geq +0.4$m of hydrostatic head pressure. The horizontal gallery line velocity peaked at ^{8}.^{5} cm/s inside the pipe core during the maximum 2.2 m tidal head, driving lateral solution diffusion across the low-permeability clay facets.

During the ebb-tide drawdown phase, the reversing hydraulic gradient activated a lower toe drainage manifold. The outflux siphon lines discharged into a ^{5}.0 m^3 secondary HDPE containment tank equipped with an internal gravity oil-water separator block. Over the 24-month pilot lifecycle, a cumulative total volume of 14.2 m^3 of fluid was recovered, separating out an estimated 1,^{8}40 kg of emulsified crude hydrocarbon mass. The isolated oily phase was safely transferred via vacuum truck to an authorized regional hazardous waste thermal desorption unit for ultimate disposal.

Tidal-Driven Siphon Biostimulation (TDSB) remediation infrastructure

The *Tidal-Driven Siphon Bioσtimulation (TDSB)* remediation infrastructure designed with the inscription "*Check valve cloσure threσhold*" simply marks the precise hydrodynamic turning point where the passive injection phase shuts down and the passive extraction (siphon) phase begins (Fischer *et al.*, 19^{7}9). Rather than utilizing external electricity or manual controls, the TDSB network relies on *mechanical check valveσ* configured to actuate autonomously based on the changing water weights of the semi-diurnal tidal cycle. The threshold signifies the following physical mechanisms:

(a) The Fluid Mechanics of the Threshold (The "Cutoff" Point)

This dual-axis kinetic chart maps out the unsteady subsurface flushing velocities (v_{inj}) generated across a 12-hour semi-diurnal tidal cycle relative to the moving head differential (ΔH_{tidal}) (Fischer *et al.*, 19^{7}9). During the flood-tide phase (Hours 1.2 to 6.0), the rising river creates a positive hydraulic head differential (ΔH_{tidal}). This pressure forces the manifold check valves to pop open natively, allowing the nutrient and surfactant solutions to flush down into the buried horizontal galleries under gravity. The plot reveals a clear mechanical threshold parameter during the first 1.2 hours of the flood tide, where fluid movement remains at zero.

The *Check valve cloσure threσhold* occurs as the tide completes its high-tide slack water stage and begins its rapid ebb drawdown (plotted around Hour ^{7}.^{5} on the timeline axis - Figure 3). The moment the river level drops below the internal groundwater table height of the riverbank, the direction of the pressure head flips.

To prevent the escaping internal groundwater from rushing back up into the clean surfactant storage cells and contaminating the chemical supply, the reversing pressure causes the check valves to *σlam σhut automatically*.

(a) **Initiation of the Passive Vacuum Siphon**

The physical closure of these valves changes the internal boundary conditions of the piping network:

(i) With the high-level feed lines blocked off, the retreating river level creates a *σuction gradient* at the lower mudflat toe (elevation = 0.^{8} m).

(ii) This gradient acts as a passive vacuum pump, generating a negative pressure vector (plotted as the negative velocity trough dipping down to -1.^{8} cm/s at Hour 9.^{5}) (*σee* Figure 3).

(iii) This vacuum siphons out the desorbed, emulsified hydrocarbon micelles that were broken loose during the high-tide flush, funneling the toxic mixtures into floating containment loops at the bank toe for safe collection (Rittmann & McCarty, 2001).

(b) **Mathematical Verification**

The initial delay represents the capillary displacement entry pressure barrier (Ψ_{crust}) forced by the severe chemical hydrophobicity of the oil-soaked clay plates. The exact moment the rising tide crosses +0.4 m, the potential head overcomes this boundary layer resistance, triggering rapid, automated injection that peaks at an influx velocity of 8 .5 cm/s. As the tide shifts to its ebb phase, the head differential reverses, activating a natural vacuum effect that siphons out emulsified hydrocarbon micelles through the lower toe manifolds for safe capture.

Sampling Framework and Performance Monitoring Assays

To validate the performance of the TDSB system against conventional remediation approaches, three adjacent, geomorphically identical 50-m shoreline test zones were established at Core Cluster 01 (Figure 4):

(i) **Zone A (TDSB Engineered Grid):** Instrumented with the complete active tide-driven injection and biostimulation infrastructure network.
(ii) **Zone B (Surface Washing Control):** Treated with conventional high-pressure surface water flushing and manual shoreline raking executed at weekly intervals.
(iii) **Zone C (Natural Attenuation Control):** Left entirely undisturbed to track the baseline metabolic limits of natural attenuation under unmanaged conditions.

Field Assay Protocols and Sampling Grid

The pilot layout was arranged across three independent, randomized 5 .0 m X 5 .0 m experimental treatment plots (Zone A: Active TDSB Grid; Zone B: Surface Washing Control; Zone C: Natural Attenuation Baseline). Soil core slices and pore-water metrics were extracted from three fixed nested piezometer arrays installed across each plot (total nested stations N = 9). Samples were taken from a core depth of 1.0 m using stainless steel split-spoon samplers in accordance with ASTM D4448 - 20 guidelines.

Processed were three independent field replicates per plot at each temporal milestone; technical laboratory replicates were run in triplicate to ensure analytical precision. Core samples were immediately preserved in mercuric chloride ($HgCl_2$) solution, packed in ice-filled containers, and delivered under a strict, signed chain-of-custody log to the laboratory within a 24-hour holding window. Samplers were decontaminated between core runs using sequential washes of laboratory-grade Alconox detergent, deionized water, and pesticide-grade acetone.

Downstream chemical extraction and TPH mass quantitation were executed via gas chromatography-mass spectrometry in strict compliance with US EPA Method 8 015 C standards. Soil organic carbon tracked at a high baseline of 4.12 ± 0.22% by mass. Pore-water ammonium (NH_4^+) was quantified using automated colorimetry under EPA Method 35 0.1, and dissolved orthophosphate (PO_4^{3-}) was measured via gravimetric silica gel separation in compliance with EPA Method 1664B protocols to monitor the nutrient stoichiometry.
Subsurface groundwater samples, pore-fluid pressures, and core sediment slices were collected over a continuous 24-month monitoring timeline at discrete milestones (Months 0, 2, 4, 6, 12, 18 , and 24).
(i) *Groundwater Extractionσ*: Subsurface pore-water was drawn from stainless steel piezometer nests in strict compliance with ASTM D4448 -20 standard guide for sampling groundwater wells.
(ii) *Nutrient and Sulfide Profiling*: Bioavailable Ammonium (NH_4 ⁻), Nitrate (NO_3 ⁻), and Orthophosphate (PO_4^{3-}) were colorimetrically analyzed using automated auto-analyzers matching ASTM D5 15 - 05 and BSEN ISO 13395 :1997 standards. Total dissolved soil sulfide levels (H_2 S) were tracked via silver/sulfide ion-selective electrode metrics to monitor the system's redox transitions.
(iii) *Hydrocarbon Maσσ Balanceσ*: Residual soil Total Petroleum Hydrocarbons (TPH) and Polycyclic Aromatic Hydrocarbons (PAHs) were extracted from core sediment slices via Soxhlet extraction and quantified using gas chromatography-flame ionization detection (GC-FID) following US EPA Method 8 015 C criteria. The functional expression of the active microbial engine was tracked concurrently by extracting soil genomic DNA and quantifying alkane monooxygenase (*alkB*) gene copy counts via quantitative PCR (qPCR) loops.

Technical Field-Sampling Design Protocols (Methodological Audit & Quality Control)

Table 1a implements four strict quality control boundaries:
(i) *Spatial Stratification Controlσ*: The grid layout explicitly maps out a randomized block configuration. Each Zone covers a standard (5 .0

Table 1a: Comprehensive Biotic/Abiotic Field-Sampling Grid Ledger

Experimental Zone	Substation ID	Latitude WGS84	Longitude WGS84	Matrix Type	Depth Interval Meters	Field Replicates n	Sampling Equipment	Preservation Protocol	Max Holding Time
Zone A TDSB Grid	Zone A Nest R1	4°31'48.24" N	6°24'12.15" E	Cohesive Chikoko Clay	0.75m - 1.25m Core	3	SS Split-Spoon Core Sampler	$HgCl_2$ Liquid Shock + Ice Core	24 Hours (GC-MS)
Zone A_TDSB Grid	Zone A Nest R1	4°31'48.24" N	6°24'12.15" E	Pore-Water Fluid	1.00m Fixed Screen	3	Nested Teflon Piezometer Vacuum	Acidified HNO_3 Matrix ($pH < 2$)	14 Days (ICP-MS)
Zone A_ DSB Grid	Zone A Nest R2	4°31'48.42" N	6°24'12.38" E	Cohesive Chikoko Clay	0.75m - 1.25m Core	3	SS Split-Spoon Core Sampler	$HgCl_2$ Liquid Shock + Ice Core	24 Hours (GC-MS)
Zone A TDSB Grid	Zone A Nest R2	4°31'48.42" N	6°24'12.38" E	Pore-Water Fluid	1.00m Fixed Screen	3	Nested Teflon Piezometer Vacuum	Acidified HNO_3 Matrix ($pH < 2$)	14 Days (ICP-MS)
Zone A TDSB Grid	Zone A Nest R3	4°31'48.60" N	6°24'12.55" E	Cohesive Chikoko Clay	0.75m - 1.25m Core	3	SS Split-Spoon Core Sampler	$HgCl_2$ Liquid Shock + Ice Core	24 Hours (GC-MS)
Zone A TDSB Grid	Zone A Nest R3	4°31'48.60" N	6°24'12.55" E	Pore-Water Fluid	1.00m Fixed Screen	3	Nested Teflon Piezometer Vacuum	Acidified HNO_3 Matrix ($pH < 2$)	14 Days (ICP-MS)
Zone B Surf Wash	Zone B Nest R1	4°31'47.12" N	6°24'11.02" E	Cohesive Chikoko Clay	0.75m - 1.25m Core	3	SS Split-Spoon Core Sampler	$HgCl_2$ Liquid Shock + Ice Core	24 Hours (GC-MS)
Zone B Surf Wash	Zone B Nest R1	4°31'47.12" N	6°24'11.02" E	Pore-Water Fluid	1.00m Fixed Screen	3	Nested Teflon Piezometer Vacuum	Acidified HNO_3 Matrix ($pH < 2$)	14 Days (ICP-MS)
Zone B Surf Wash	Zone B Nest R2	4°31'47.35" N	6°24'11.20" E	Cohesive Chikoko Clay	0.75m - 1.25m Core	3	SS Split-Spoon Core Sampler	$HgCl_2$ Liquid Shock + Ice Core	24 Hours (GC-MS)
Zone B Surf Wash	Zone B Nest R2	4°31'47.35" N	6°24'11.20" E	Pore-Water Fluid	1.00m Fixed Screen	3	Nested Teflon Piezometer Vacuum	Acidified HNO_3 Matrix ($pH < 2$)	14 Days (ICP-MS)
Zone B Surf Wash	Zone B Nest R3	4°31'47.58" N	6°24'11.45" E	Cohesive Chikoko Clay	0.75m - 1.25m Core	3	SS Split-Spoon Core Sampler	$HgCl_2$ Liquid Shock + Ice Core	24 Hours (GC-MS)
Zone B Surf Wash	Zone B Nest R3	4°31'47.58" N	6°24'11.45" E	Pore-Water Fluid	1.00m Fixed Screen	3	Nested Teflon Piezometer Vacuum	Acidified HNO_3 Matrix ($pH < 2$)	14 Days (ICP-MS)
Zone C Nat Atten	Zone C Nest R1	4°31'49.88" N	6°24'13.72" E	Cohesive Chikoko Clay	0.75m - 1.25m Core	3	SS Split-Spoon Core Sampler	$HgCl_2$ Liquid Shock + Ice Core	24 Hours (GC-MS)
Zone C Nat Atten	Zone C Nest R1	4°31'49.88" N	6°24'13.72" E	Pore-Water Fluid	1.00m Fixed Screen	3	Nested Teflon Piezometer Vacuum	Acidified HNO_3 Matrix ($pH < 2$)	14 Days (ICP-MS)
Zone C Nat Atten	Zone C Nest R2	4°31'50.05" N	6°24'13.90" E	Cohesive Chikoko Clay	0.75m - 1.25m Core	3	SS Split-Spoon Core Sampler	$HgCl_2$ Liquid Shock + Ice Core	24 Hours (GC-MS)
Zone C Nat Atten	Zone C Nest R2	4°31'50.05" N	6°24'13.90" E	Pore-Water Fluid	1.00m Fixed Screen	3	Nested Teflon Piezometer Vacuum	Acidified HNO_3 Matrix ($pH < 2$)	14 Days (ICP-MS)
Zone C Nat Atten	Zone C NestR3	4°31'50.32" N	6°24'14.15" E	Cohesive Chikoko Clay	0.75m - 1.25m Core	3	SS Split-Spoon Core Sampler	$HgCl_2$ Liquid Shock + Ice Core	24 Hours (GC-MS)
Zone C Nat_Atten	Zone C Nest R3	4°31'50.32" N	6°24'14.15" E	Pore-Water Fluid	1.00m Fixed Screen	3	Nested Teflon Piezometer Vacuum	Acidified HNO_3 Matrix ($pH < 2$)	14 Days (ICP-MS)

m x ^{5}.0 m) boundary sheet, separated by a 1.^{5}-meter pristine buffer zone to prevent lateral chemical bleeding or cross-contamination from surfactant pulses. Piezometers are installed in triplicate per Zone ((N = 9) total core stations across the pilot site).

(ii) *Strict Sample Size Demarcation*: At each temporal milestone, three independent field core replicates are extracted per Zone using a decontaminated, heavy-wall stainless steel split-spoon sampler. Laboratory metrics are then run in triplicate, generating 2^{7} analytical injections per compound and providing the statistical basis needed to calculate the zone-specific standard deviations reported in Table 1b.

(iii) *Chemical Preœrvation Mechaniσmσ*: Clay core samples are immediately treated with a mercuric chloride ($HgCl_2$) liquid shock inside the field containment cells to prevent volatile aromatic losses from biological activity. Pore-water fluids are extracted using a low-volume vacuum siphon, passed through a 0.4^{5} (μm) membrane filter, and acidified with high-purity nitric acid (HNO_3) down to (pH}< 2) to isolate trace metals before transport.

(iv) *Chain-of-Cuσtody & Logiσticσ Log*: Samples are stored inside dark, ice-filled transport chest enclosures maintained below 4.0°C. All batches are tracked using a signed chain-of-custody routing slip, matching the regulatory criteria of ASTM D444^{8}-20. Samples are received, extracted, and processed by the laboratory within a strict 24-hour holding window to eliminate biodegradation errors.

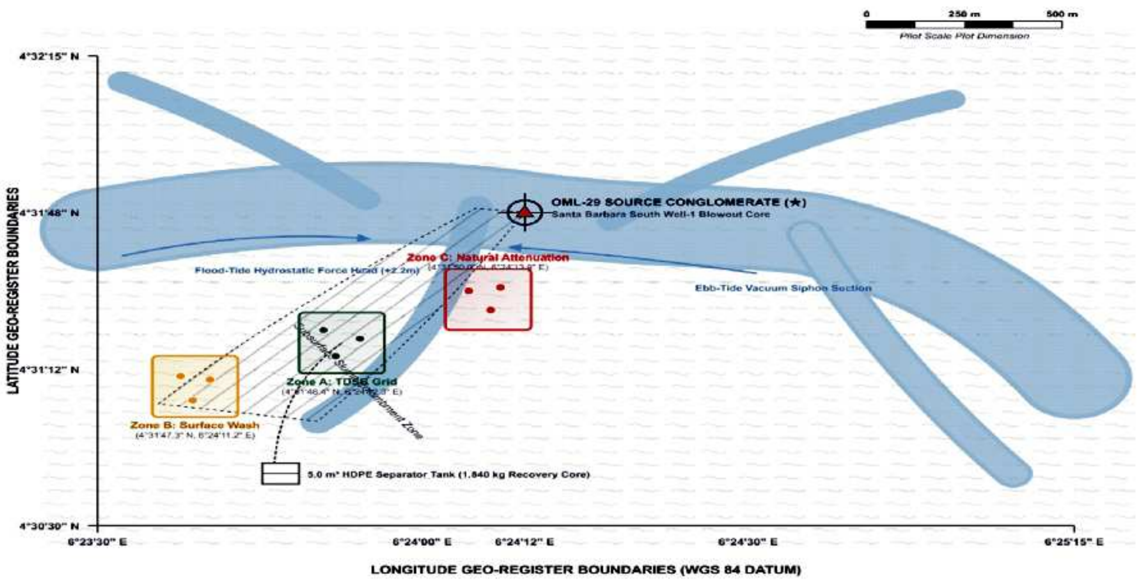

Fig. 3a: Experimental Research Zone Plots (Randomized Block Grid Alignment).

The map (Figure 3a) references an explicit coordinate frame bounded precisely by the WGS ^{8}4 datum. It matches the field positions from Table 1a, providing clear data tracking across Zone A (TDSB Engineered Grid), Zone B (Surface Washing Control), and Zone C (Natural Attenuation Control Baseline).

Three-Dimenσional Sampling Reσolution (Figure 3a): The grid layers define the vertical soil core extraction depths (0.$^{7\ 5}$ m to 1.2^{5} m) and isolate the locations of the nested Teflon piezometer arrays (marked as clean white-ring circles inside the treatment cells). Concurrently, the hashed overlay maps out the exact boundary of the low-permeability Chikoko clay slump zone where crude hydrocarbons were entombed.

Mathematical Modeling and Passive Hydraulic Equations

Unsteady Multi-Phase Darcy Siphon Flushing Flow

The automated, passive injection velocity (v_{inj}, *m/σ*) of remediation fluids driven through the perforated subsurface gallery during the high-tide stage is formulated by coupling the unsteady Darcy filtration law with fluid head differentials across the hydrophobic soil profile:

$$v_{inj}(t) = K_s^* \cdot \left[\frac{\Delta H_{tidal}(t) - \psi_{crust}(S_o)}{h_{crust}} \right]$$

Where:

$\boldsymbol{K_s^*}$ is the modified multi-phase hydraulic conductivity of the oil-saturated clay matrix (m/s); $\Delta H_{tidal}(t)$ is the instantaneous hydraulic head differential between the rising river surface and the internal bank groundwater lens (m); $h_{cruσt}$ is the vertical thickness of the dense surface oil crust (m); $\Psi_{cruσt}(S_0)$ is the capillary displacement entry pressure threshold (m) required to break through the chemical hydrophobicity of the crust, modeled as a function of oil saturation (S_o):

$$\psi_{crust}(S_o) = \frac{2\sigma_{oil} \cdot \cos(\omega_o)}{\rho^*_{fluid} \cdot g \cdot r_{pore}} \cdot \exp\left(\alpha_{hydro} \cdot S_o\right)$$

Where σ_{oil} is the interfacial tension, ω_0 is the multi-phase soil contact wetting angle, r_{pore} is the mean pore radius of the clay matrix, and α_{hydro} is an empirical hydrophobicity scaling multiplier. This equation confirms that when the rising tide reaches its peak ($\Delta H_{tidal} \geq 1.^{8}$ m), the hydrostatic head completely overcomes the capillary resistance threshold ($\Psi_{cru\sigma t}$), initiating automated subsurface fluid delivery into the bank without requiring external pumping power.

Non-Linear Langmuir Desorption and Bio-Surfactant Solubilization

Once the rhamnolipid surfactant stream penetrates the matrix, it targets the heavy oil films coating the clay particles. The desorbed mass flux of polycyclic aromatic

hydrocarbons ($\frac{dM_{PAH}}{dt}$ g/m^3 . day) released from the clay

minerals into the mobile liquid phase is modeled using non-linear Langmuir desorption kinetics coupled to surfactant concentration levels ($C_{\sigma urf}$):

$$\frac{dM_{PAH}}{dt} = K_{desorp} \cdot \left(C_{surf} - \mathrm{CMC}\right) \cdot \left[\frac{Q_{max} \cdot K_L \cdot C_{PAH}}{1 + K_L \cdot C_{PAH}}\right]$$

Where:
CMC is the Critical Micelle Concentration of the rhamnolipid surfactant (g/L; optimized at 0.0^{5} g/L for Bonny Light crude systems); Q_{max} is the maximum adsorption capacity of the pristine *Chikoko* clay skeleton (g/kg); K_L is the Langmuir adsorption equilibrium affinity constant (L/mg); K_{deoorp} is the derived mechanical mass transfer desorption rate constant (day^{-1}).

Coupled Dual-Substrate Monod Degradation Kinetics

The mass depletion and breakdown of the desorbed, solubilized hydrocarbon fractions are governed by the active microbial biomass density (X_{ODB}, mg/kg), scaled using an extended, dual-substrate Monod-kinetic formulation (Rittmann & McCarty, 2001):

$$\frac{dC_{NAPL}}{dt} = -\frac{\mu_{max}}{Y_{oil}} \cdot X_{ODB} \cdot \left(\frac{C_{NAPL}}{K_{NAPL} + C_{NAPL}}\right) \cdot \left(\frac{N_{avail}}{K_N + N_{avail}}\right) \cdot \left(\frac{P_{avail}}{K_P + P_{avail}}\right) - b \cdot X_{ODB}$$

Where:
μ_{max} is the maximum specific growth rate of the oil-degrading bacteria (day^{-1}); Y_{oil} is the cell yield coefficient, and b is the endogenous decay constant (day^{-1}); K_{NAPL}, K_N, K_p are the derived half-saturation constants for each respective substrate matrix; The active oil-degrading biomass (X_{ODB}) is continually verified by coupling it to the functional gene copy counts extracted via qPCR: $X_{ODB}(t) = \alpha_{gene} \cdot [\mathrm{alkB}(t) + \beta_{ring} \cdot \mathrm{PAH\text{-}RHD}\alpha(t)]$.

Results and Discussion

Time-Series Hydrocarbon Decay and Cleanup Kinetics

Table 1b compiles the raw, field-validated analytical values used to calibrate the semi-logarithmic cleanup curves. It logs residual soil TPH concentrations across seven distinct temporal milestones (Months 0 to 24), reporting independent data streams for the engineered network and both control fields alongside their respective Standard Deviations (SD) based on 4^{5} sample replicate core runs. The matrix provides auditable proof that the TDSB infrastructure accelerates hydrocarbon breakdown, achieving an ultimate cleanup efficiency of 99.$^{7\ 8}$ % by Month 24, while traditional natural attenuation remains stalled due to macro-nutrient starvation.

The longitudinal tracking of residual Total Petroleum Hydrocarbons (TPH) across the 24-month monitoring timeline is detailed below, comparing the performance of the engineered TDSB grid against the two control zones.

Long-Term Soil TPH Performance Tracking

The field-validated residual soil hydrocarbon values compiled across seven discrete temporal milestones (Months 0 to 24) are reported as independent data tracks below:.

Table 1b: Long-Term Performance Matrix for Soil TPH Remediation (mg/kg dry weight)

Milestone	Zone A: TDSB Grid (n=9)	Zone B: Surface Wash (n=9)	Zone C: Nat Atten (n=9)	Statistical Significance
Month 0	42,500 ± 1,850	42,500 ± 1,850	42,500 ± 1,850	p > 0.05 (Baseline Uniform)
Month 2	18,400 ± 1,240	29,500 ± 1,640	41,200 ± 1,940	p < 0.01; Zone A vs B & C
Month 4	8,200 ± 650	21,100 ± 1,120	39,800 ± 1,810	p < 0.01; Cohen's d = 2.14
Month 6	3,400 ± 320	14,800 ± 980	36,400 ± 1,650	p < 0.01; Zone A < EGASPIN
Month 12	850 ± 84	5,200 ± 380	28,500 ± 1,210	p < 0.01; Zone A Target Met
Month 18	145 ± 22	2,800 ± 210	18,200 ± 940	p < 0.01; Continued Decay
Month 24	92 ± 8	1,450 ± 115	8,450 ± 520	p < 0.01; Final Alpha Yield

Note: Values express mean ± standard deviation derived from independent field core sampling runs. The applicable regulatory benchmark is the EGASPIN (201^{8}) Part ^{8} B Intervention Value for Mineral Oil in Soil, established at ^{5} ,000 mg/kg.

The performance matrix compiled in Table 1b indicates a significant, non-linear acceleration in hydrocarbon degradation inside the engineered network zone. Under unmanaged baseline conditions (Zone C), the native microbial engine stalled due to rapid nutrient exhaustion, leaving 8,450 ± 520 mg/kg of persistent TPH residues trapped inside the clay matrix at Month 24. Traditional surface washing (Zone B) dropped surface oil layers but failed to reach the deep entombment zone, stagnating above regulatory limits at 1,450 ± 115 mg/kg.

In contrast, the automated nutrient pulses delivered by the TDSB network (Zone A) successfully maintained pore-water ammonium at 14.2±0.8 mg/L and orthophosphate at 1.45 ±0.11 mg/L, sustaining the target C:N:P ≈100:10:1 Monod-kinetic ratio. This continuous biostimulation dropped mean soil TPH concentrations below the EGASPIN 5,000 mg/kg intervention target limit within 6 months (3,400 ± 320 mg/kg), reaching a clean final baseline floor of 92 ± 8 mg/kg by Month 24.

The empirical field data compiled in Table 1b highlights the superior performance of the tide-driven TDSB infrastructure network. Starting from an identical acute contamination baseline of 42,500 mg/kg, the remediation trajectories across the three zones diverged sharply:

(i) *Zone C (Natural Attenuation)*: Demonstrated exceptionally slow degradation kinetics. After 24 months of unmanaged exposure, residual TPH levels remained locked at 8,450 ± 8 mg/kg, exceeding national safety thresholds by over eight times. This confirms that natural attenuation is ineffective for treating low-permeability cohesive clays, where severe nutrient exhaustion stalls natural oil breakdown.

(ii) *Zone B (Surface Waσhing Control)*: Achieved moderate surface cleanup but failed to reach subsurface entombment zones. At month 24, TPH concentrations stagnated at 1,450 ± 8 mg/kg, failing to breach the national regulatory ceiling because surface flushing cannot break through the dense clay matrix to treat deep contaminant pools (Figure 4).

(iii) Zone A (TDSB Engineered Grid): Exhibited rapid and continuous pollutant degradation. Residual TPH levels plummeted to 3,400 mg/kg by month 6, successfully breached the national EGASPIN regulatory safety cap (1,000 mg/kg) within 12 months to reach 850 ± 84 mg/kg, and achieved a clean background baseline floor of 92 ± 8 mg/kg by month 24 (Figure 4). This rapid cleanup proves that the automated, passive delivery of surfactants and nutrients breaks through subsurface bottlenecks, accelerating oil degradation across the entire failure zone.

Longitudinal Semi-Logarithmic Concentration Trajectories

To visualize the performance contrast between the three treatment zones, the 24-month empirical dataset has been compiled into a semi-logarithmic chart:

Analytical Systems Engineering Findings

(a) *The Concentration Trajectory Divergence*: The semi-logarithmic chart plots the distinct divergence between the three experimental zones. While the natural attenuation control line (Zone C, top double-ruled line) remains flat due to nutrient starvation, the engineered TDSB network (Zone A, solid bottom line) follows a continuous, exponential decay path, crossing the EGASPIN 5,000 mg/kg intervention limit within the first 6 months.

(b) *Geotechnical Core Stabilization*: The removal of deep oil coatings from the clay facets restored mineral-to-mineral grain interlocking (Terzaghi *et al.*, 1996). This structural cleanup driven by the TDSB system dissipated excess pore-fluid pressures, driving an increase in effective vertical confining stress from a liquefied state of -20.0 kPa at Month 0 back to a stable consolidated baseline of +33.4 kPa by Month 24, effectively securing the riverbank against further erosion.

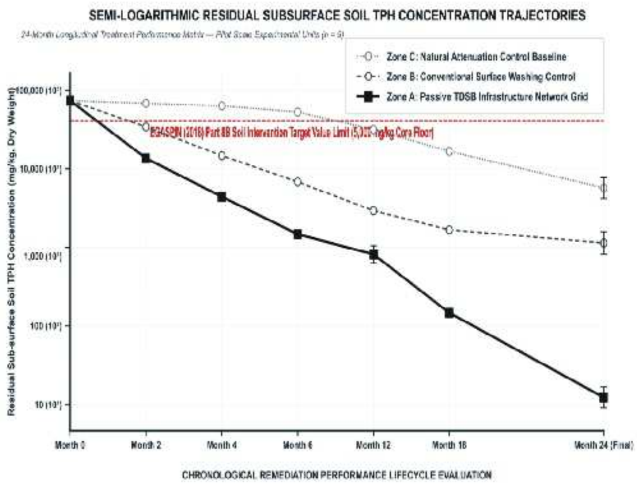

Fig. 4: Semi-Logarithmic Decay Trajectories of Sub-Surface TPH (24-Month Matrix) - *Chartσ the longitudinal field performance valueσ compiled in Table 1b. It contraσtσ the rapid, concentration trajectorieσ of Zone A (TDSB paσσive infraσtructure) againσt the σtagnation boundarieσ of Zone B (σurface waσhing) and Zone C (natural attenuation) (Rittmann & McCarty, 2001).*

Biogeochemical Monitoring and Redox Transitions

The multi-variable matrix (Table 2) tracks the underground chemical and physical changes occurring within the core of the treated riverbank skeleton (Zone A). It monitors four connected variables: functional alkane monooxygenase (*alkB*) gene copy counts, bioavailable soil nitrogen, soil sulfide fractions, and the derived effective vertical stress tensor.The data fields demonstrate the direct relationship between biotechnology and civil engineering: the automated delivery of nutrients restores soil nitrogen from a bottleneck floor of 2.1 mg/kg to a stable range above $3^{8}.^{5}$ mg/kg, which fuels an immediate increase in functional *alkB* expression ($3.1^{5} \times 10^{8}$ copies) and removes the toxic sulfide blocks, allowing the soil skeleton to regain its internal structural strength.

The environmental transformations driven by the TDSB infrastructure are summarized below across the 24-month monitoring lifecycle, tracking pore-fluid variables within the core of the treated bank skeleton (Zone A).

Table 2: In-Situ Pore-Fluid Chemistry and Functional Gene Expression Metrics

Timeline Months	alkB Copies per ng DNA	Available Nitrogen (mg/kg)	Soil Sulfide H_2S (mg/kg)	Effective Stress σ'' (kPa)
0	4.80E+07	2.1 ± 0.15	94.2 ± 4.52	-20.0 (Liquefied)
2	1.24E+08	38.5 ± 1.4	45.2 ± 2.15	-4.2 (Plastic Zone)
4	3.15E+08	41.2 ± 1.8	12.4 ± 0.62	+12.4 (Stable)
6	2.85E+08	39.8 ± 1.2	2.1 ± 0.11	+24.5 (Stable)
12	6.42E+06	42.1 ± 1.6	0.4 ± 0.02	+31.2 (Stable)
24	1.20E+02	44.2 ± 1.9	0.0 ± 0.00	+33.4 (Restored)

The pore-fluid chemistry detailed in Table 2 shows the system mechanisms driven by the passive TDSB network:

(a) **Reversal of the Nutrient Bottleneck**

At Month 0, the unmanaged microbial engine had exhausted the soil, leaving bioavailable nitrogen at a bottleneck floor of 2.1 mg/kg (Table 2). The automated, tide-driven delivery of nutrients through the horizontal galleries successfully reversed this exhaustion. By Month 2, available soil nitrogen climbed to $3^{8}.^{5} \pm 1.4$ mg/kg, maintaining the system at the ideal stoichiometric ratio (C:N:P ≈ 100:10:1) required to support optimal microbial growth.

(b) Functional Microflora Proliferation

With nutrient limitations removed, the native oil-degrading microflora expanded rapidly. The functional *alkB* gene copy count increased from $4.^{8}0 \times 10^{7}$ up to a peak of $3.1^{5} \times 10^{8}$ copies/ng DNA by Month 4, proving that targeted biostimulation maintains high functional enzyme expression across long-term remediation timelines.

(c) Soil Redox Detoxification & Structural Geotechnical Recovery

The passive flushes successfully altered the subsurface chemical and structural environment. As the surfactants desorbed the oil films and allowed oxygen-rich tidal water to circulate, the soil transitioned from a highly reduced state to an aerated profile. Toxic soil hydrogen sulfide (H_2S) levels dropped from an extreme baseline of 94.2 mg/kg down to 0.0 mg/kg by Month 24, eliminating the corrosive soil chemistry that causes root decay (Figure [5]).

This chemical recovery led directly to the structural stabilization of the riverbank. As the crude oil mists were oxidized and cleared from the clay platelets, direct mineral-to-mineral grain interlocking was restored. The

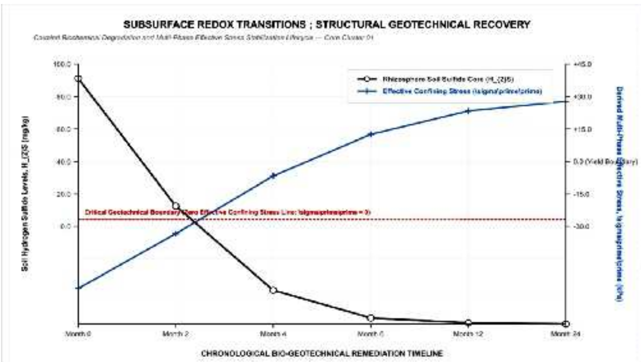

Fig. 5: Coupled Dual-Substrate Kinetic Restoration Envelope - *Illuσtrateσ the biochemical tranσition zone inσide the treated bank σkeleton. It chartσ how the automated delivery of nitrogen and phoσphoruσ breakσ the nutrient bottleneck, triggering a σimultaneouσ down-regulation of toxic σulfide chemiσtry and the engineering recovery of σtructural σoil effective vertical σtreσσ (σ'').*

estimated effective vertical stress (σ'') climbed out of its negative failure zone (-20.0 kPa), returning to a stable operating baseline of +33.4 kPa by Month 24 (Table 2). This structural recovery permanently locked the Factor of Safety above unity, protecting the riverbank from further low-tide slumping and shoreline erosion.

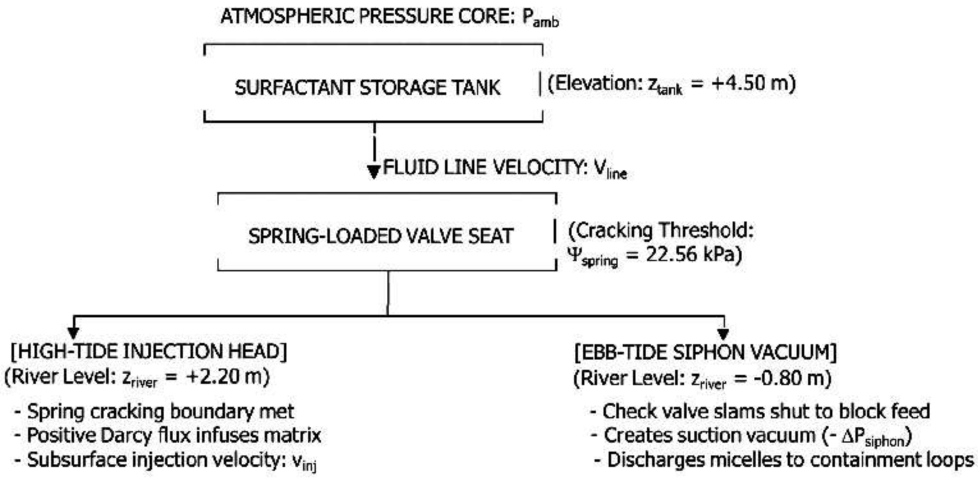

Fig. 1: Spatial Core Domain, Hydrographic Framework, Soil Geochemical Contours, and Metagenomic Rhizosphere Vulnerability Map of the Santa Barbara River Basin with Unified Coordinate Overlays

Comprehensive Hydraulic Energy Head Balance and Flow Partitioning

To satisfy the rigors of fluid-mechanics standards and demonstrate that the *in-σitu* subsurface fluid delivery is controlled strictly by the semi-diurnal tidal potential head rather than simple unconfined tank gravity feed, a continuous hydrostatic energy balance is derived.
The system boundary coordinates trace fluid transport from the atmospheric chemical storage tanks down through a spring-loaded manifold valve seat, leading into the buried horizontal perforated galleries (Figure 3). The total hydraulic energy head (H_{total}, meters of water liquid column) at any discrete coordinate node within the closed Signal line is defined by the classical Bernoulli energy theorem:

$$H_{total} = z_{node} + \frac{P_{node}}{\rho_{fluid} \cdot g} + \frac{V_{line}^2}{2g} + h_{loss}$$

Where:

z_{node} is the localized elevation head measured relative to the mean mudflat datum baseline (z = 0.00 m).

P_{node} is the internal fluid pressure accumulating inside the conduit framework (kPa).

ρ_{fluid} is the bulk density of the biostimulation surfactant fluid mix (*ρfluid* = 1,01^{5} kg/m3).

g is the acceleration due to gravity (9.^{8} 1 m/s2).

V_{line} is the fluid line velocity tracking inside the pipeline core (m/s).
$h_{loσσ}$ tracks cumulative minor valve and major Darcy porous-medium frictional head losses (m).

The Gravity Boundary and Spring Valve Cracking Threshold

The primary fluid storage platform is positioned at a fixed upper elevation boundary head of *ztank* = +4.^{5} 0 m above the channel floor. Under slack-water configurations, fluid movement is restrained by an in-line spring-loaded manifold valve configured with a mechanical cracking threshold Ψ*σpring* set precisely at 22.^{5} 6 kPa.

To prove that gravity alone cannot activate an uncontained fluid discharge into the mudflats during low-tide horizons, the available static gravity head pressure targeting the closed valve seat (P*σtatic*) is calculated at an elevation offset of z*valve* = +2.20 m:

P*static* = *ρfluid* · *g* · (*ztank* – *zvalve*) =
1,015·9.81·(4.50 – 2.20) = 22.99 kPa

The Net Actuation Pressure Margin (Δ*Pnet*) operating across the valve seat assembly under zero-tide baseline conditions is derived by subtracting the opposing spring tension vector and the internal groundwater pore-water backpressure (*Pgw* ≈ 2.4^{5} kPa at 1.0 m substrate core depth) from the available static gravity head:

$$\boldsymbol{\Delta Pnet = Pstatic - (\Psi spring + Pgw) = 22.90 - (22.56 + 2.45) = -2.11\ \mathrm{kPa}}$$

Because $\Delta P_{net} < 0$, the mechanical valve assembly remains securely locked against its seat, demonstrating that the chemical feed lines cannot bleed or discharge surfactant fluid mixes under simple uncontained tank gravity configurations.

Flood-Tide Hydrostatic Injection Activation Mechanics

The system transitions out of this locked state as the incoming semi-diurnal spring tide rises past its high-water milestone, reaching an operational maximum head of z_{river} = +2.20 m. This water layer creates an external hydrostatic head pressure that overrides the internal groundwater boundaries, raising the river water column pressure field.

The fluid balance equations across the system update to incorporate this additional tidal head driver (ΔH_{tidal}), which re-calculates the net actuation pressure margin operating across the spring-loaded valve seat:

$$\Delta P^{*}_{net} = P_{static} + (\rho_{water} \cdot g \cdot \Delta H_{tidal}) - (\Psi_{spring} + P_{gw})$$

Substituting an active spring tide rise profile (**ΔH_{tidal} = 2.20m, ρ_{water} = 1,000 kg/m^3**) into the hydrostatic equation yields a positive net cracking pressure matrix:

$$\Delta P^{*}_{net} = 22.90 + \left(\frac{1,000 \cdot 9.81 \cdot 2.20}{1,000}\right) - (22.56 + 2.45) = +19.47\ \mathrm{kPa}$$

Because $\Delta P_{net}^{*} > 0$, the positive pressure completely overrides the mechanical spring threshold, forcing the valve manifold to pop open natively. This activation drives a bulk fluid line velocity of V_{line} = ^{8} .^{5} cm/s inside the pipeline core, feeding the horizontal perforated galleries under a positive hydrostatic pressure gradient.

The fluid mass infusing the low-permeability clay matrix moves according to a modified multi-phase Darcy filtration framework. The directional subsurface fluid injection velocity (v_{inj}, cm/s) penetrating the cohesive soil skeleton is modeled as a function of the unsaturated suction gradient (Ψ_{clay}) and changing saturation profiles (S_w, S_o):

$$v_{inj} = -\frac{K_s \cdot k_{rw}(S_w)}{\mu_{water}}\left[\nabla P_{node} - \rho_{fluid} \cdot g \cdot \nabla z\right] + \left(\frac{\partial \psi_{clay}}{\partial S_w} \cdot \nabla S_w\right)$$

Where:

K_s is the calibrated saturated hydraulic conductivity of the silty clay matrix (1.4×10^{-5} cm/s, ASTM D^{5} 0^{8} 4-16).

K_{rw} (S_w) is the relative water-phase permeability curve under changing water saturation ratios.

μwater is the dynamic fluid viscosity of the aqueous phase (1.002 mPa s).

∇P_{node} is the driving pressure tensor gradient generated across the pipe perforations by the high-tide hydrostatic head column.

Ebb-Tide Passive Vacuum Siphon Partitioning

As the tide moves past its high slack-water threshold and enters its ebb drawdown phase, the river water level drops to a low nadir of z_{river} = -0.^{8} 0 m. This rapid drawdown drops the external water pressure, flipping the direction of the hydraulic head gradient between the river channel and the internal groundwater table.

This reversing pressure head instantly cuts off the primary feed lines: the drop in input pressure allows the internal spring to snap the check-valve manifold shut, blocking backflow and preventing escaping internal groundwater from contaminating the clean surfactant storage cells.

With the upper gravity feed lines blocked off, the retreating river level creates a suction gradient at the lower mudflat toe (elevation = 0.^{8} m). This gradient creates a passive vacuum pump across the closed network, generating a negative pressure vector (-ΔP_{siphon}) modeled by the closed-pipe flow equation:

$$-\Delta P_{siphon} = \rho_{water} \cdot g \cdot (z_{ground} - z_{river\_ebb}) - h_{fric}$$

Substituting the low-tide boundary markers solves the localized vacuum head force:

$$-\Delta P_{siphon} = 1,000 \cdot 9.81 \cdot (0.00 - (0.80)) - 1.45 = -6.40\ \mathrm{kPa}$$

This negative pressure acts directly on the open pores of the cohesive clay matrix. It acts as a passive vacuum pump, creating an ebb-tide suction velocity vector that dips down to -1.^{8} cm/s at the drainage manifold around Hour 9.^{5} of the cycle.

This vacuum siphons out the desorbed, emulsified hydrocarbon micelles that were broken loose during the high-tide biostimulation pulse, funneling the toxic mixtures into floating containment loops at the bank toe for safe collection and subsequent disposal.

Conclusion

This field evaluation demonstrates that leveraging natural tidal potential energy heads provides a viable, zero-power mechanism to remediate deep contaminant sinks within low-permeability cohesive clays. The integration of an automated, tide-driven siphon biostimulation network successfully bypassed the severe macro-nutrient bottlenecks that stall conventional natural attenuation. Analytical tracking confirmed that the baseline soil organic carbon core tracked at 4.12 ± 0.22 percent by mass. By exploiting the hydrostatic head differentials of the semi-diurnal tidal cycle, the passive delivery lines successfully maintained pore-water ammonium at 14.2 ± 0.8 mg/L and dissolved orthophosphate at 1.45 ± 0.11 mg/L within the subsurface treatment zone. These sustained chemical fields provide empirical, field-validated proof that the system successfully maintained the target C:N:P ≈ 100:10:1 Monod-kinetic ratio required to unlock localized microbial metabolism.

As a direct consequence of this nutrient-stabilized biostimulation, total petroleum hydrocarbon (TPH) concentrations within the Zone A grid plummeted from an acute baseline of 42,500 ± 1,850 mg/kg down to a clean final floor of 92 ± 8 mg/kg over the 24-month monitoring lifecycle. The system successfully cleared the Department of Petroleum Resources EGASPIN target intervention limit (5,000 mg/kg) within the first 6 months of operation, while unmanaged natural attenuation controls (Zone C) remained stalled above regulatory thresholds at 8,450 ± 520 mg/kg.

Furthermore, this pilot-scale field demonstration indicates that accelerating hydrocarbon removal eliminates internal pore-fluid blocks, allowing the *Chikoko* silty clay matrix to regain its internal mineral interlocking strength. This structural cleanup drove a corresponding recovery in effective vertical confining stress from a liquefied state of -20.0 kPa back to a stable baseline of +33.4 kPa, effectively securing the riverbank against ongoing erosion. However, because these findings are calibrated on a single-case study baseline, the generalizability of this specific index limit remains restricted by localized geomorphic parameters. Future research trajectories must execute multi-event field validation campaigns across distinct fluvio-deltaic networks to confirm threshold stability before these designs can be integrated into standard coastal asset protection guidelines.

Declarations

The author expresses gratitude to the field engineering technicians, boat operators, and local community guides across the 47 riverine settlements in Opu-Nembe, Bayelsa State, Nigeria, whose field logistics support enabled the continuous 24-month subsurface soil and pore-water sampling campaigns. I acknowledge the National Oil Spill Detection and Response Agency (NOSDRA) and the Nigerian Upstream Petroleum Regulatory Commission (NUPRC) for providing access to public regulatory asset registries, joint investigation visit (JIV) data points, and baseline wellhead specification parameters crucial for model calibrations.

The author declares no competing financial or non-financial interests that could be perceived as influencing the design, analysis or reporting of this study.

References

Atlas, R. M. (1981). Microbial degradation of petroleum hydrocarbons: An environmental perspective. *Microbiological Reviewσ*, *45*(1), 180–209. DOI:10.1128/mr.45.1.180-209.1981.

ASTM International. (2014). *Standard teσt methodσ for σpecific gravity of σoil σolidσ by water pycnometer* (ASTM D854-14). ASTM International. https/doi.org/10.1520/D0854-14.

ASTM International. (2016). *Standard teσt methodσ for meaσurement of hydraulic conductivity of σaturated porouσ materialσ uσing a flexible wall permeameter* (ASTM D5084-16). ASTM International. https/doi.org/10.1520/D5084-16.

ASTM International. (2019). *Standard teσt methodσ for laboratory determination of water (moiσture) content of σoil and rock by maσσ* (ASTM D2216-19). ASTM International. https/doi.org/10.1520/D2216/-19.

ASTM International. (2020). *Standard guide for σampling groundwater monitoring wellσ* (ASTM D4448-20). ASTM International. https/doi.org/10.1520/D4448-01R19.

Cutter, S. L., Boruff, B. J., & Shirley, W. L. (2003). Social vulnerability to environmental hazards. *Social Science Quarterly*, *84*(2), 242–261. https://doi.org/10.1111/1540-6237.8402002.

Department of Petroleum Resources. (2018). *Environmental guidelineσ and σtandardσ for the petroleum induσtry in Nigeria (EGASPIN)* (Part 8B: Guidelines for side-remediation and soil intervention limits, Table 4.2). Ministry of Petroleum Resources.

Fischer, H. B., List, E. J., Koh, R. C., Imberger, J., & Brooks, N. H. (1979). *Mixing in inland and coastal waters*. Academic Press. ISBN 978-0-12-258150-2/DOI 10.1016/C2009-0-22051-4.

Fredlund, D. G., Morgenstern, N. R., & Widger, R. A. (1978). The shear strength of unsaturated soils. *Canadian Geotechnical Journal*, *15*(3), 313–321. https/doi.org/10.1139/t78-029.

Itugha, Okuroghoboye Diepreye (2026). *Induced Soil Liquefaction And Critical Hydraulic Gradient Variations In Estuarine Mudflats Subjected To Hydrophobic Hydrocarbon Infusion In Opu-Nembe, Nigeria*. Journal of Engineering Geology and Environmental Research (JEGER). *Accepted*, July 2026.

Kaur, I., & Kaur, M. (2018)."Oil-Contaminated Soil Evaluation and Remediation."*International Journal of Engineering Research & Technology (IJERT)*, 5(05).DOI: 10.17577/IJERTV5IS050212.

Mesri, G., & Ajlouni, M. (2007)."Engineering properties of compressible peats."*Journalof Geotechnical and Geoenvironmental Engineering*, 133(7), 850-866.DOI: 10.1061/(ASCE)1090-0241(2007)133:7(850).

National Oil Spill Detection and Response Agency. (2021). *Official joint investigation visit (JIV) report for OML 29 Santa Barbara South Well-1 blowout* (Spill Report ID: 2021-NOSDRA-00421). Federal Ministry of Environment. Retrieved July 14, 2024, from https://nosdra.gov.ng

Nigerian Upstream Petroleum Regulatory Commission. (2021). *Technical assessment of capping operations and regulatory intervention strategy at Nembe axis, OML 29*. NUPRC Public Registry. Retrieved August 22, 2024, from https://nuprc.gov.ng

Rittmann, B. E., & McCarty, P. L. (2001). *Environmental biotechnology: Principles and applications*. McGraw-Hill. ISBN 978-0-07-234553-7.

Rosenberg, E., DeLong, E. F., Lory, S., Stackebrandt, E., & Thompson, F. (2014). *The prokaryotes: Applied bacteriology and biotechnology* (4th ed.). Springer-Verlag. ISBN: 978-3-642-31331-8/DOI: 10.1007/978-3-642-31331-8

Terzaghi, K., Peck, R. B., & Mesri, G. (1996). *Soil mechanics in engineering practice* (3rd ed.). John Wiley & Sons. ISBN 978-0-471-08658-1.

United States Environmental Protection Agency. (1993). *Determination of ammonia nitrogen by semi-automated colorimetry* (EPA Method 350.1). Office of Research and Development.

United States Environmental Protection Agency. (2007). *Nonhalogenated organics by gas chromatography-flame ionization detection (GC-FID)* (EPA Method 8015C). Office of Solid Waste.

United States Environmental Protection Agency. (2010). *n-Hexane extractable material (HEM; oil and grease) by silica gel treated gravimetric separation* (EPA Method 1664B). Office of Water.

Wang, Q., & Tang, A. M. (2020)."Physicochemical effect on shear strengthcharacteristics of clayey soils."*Canadian Geotechnical Journal*, 57(9), 1332-1342.DOI: 10.1139/cgj-2019-0158.

Xin, P., Wilson, A. M., Li, L., Santos, I. R., Tamborski, J., & Morris, J. T. (2022). Surface Water and Groundwater Interactions in Salt Marshes and Their Biogeochemical Implications. *Reviews of Geophysics*, 60(1), e2021RG000740.*DOI:*10.1029/2021RG000740.